Applied Catalysis B: Environmental 243 (2019) 273–282

Contents lists available at ScienceDirect

Applied Catalysis B: Environmental

journal homepage: www.elsevier.com/locate/apcatb

Catalytic application of ferrierite nanocrystals in vapour-phase dehydration of methanol to dimethyl ether

Enrico Catizzone[a,*], Stijn Van Daele[b], Micaela Bianco[a], Alessandro Di Michele[c], Alfredo Aloise[a], Massimo Migliori[a], Valentin Valtchev[b,d,**], Girolamo Giordano[a]

[a] Department of Environmental and Chemical Engineering, University of Calabria, Via P. Bucci, I-87036, Rende, CS, Italy
[b] Normandie Univ., ENSICAEN, UNICAEN, CNRS, Laboratoire Catalyse et Spectrochimie, 14000, Caen, France
[c] Department of Physics and Geology, University of Perugia, via Pascoli, 1-06123, Perugia, Italy
[d] State Key Laboratory of Inorganic Synthesis and Preparative Chemistry, Jilin University, Changchun, 130012, China

ARTICLE INFO

Keywords:
Ferrierite
Crystal morphology
Brønsted-Lewis acidity
Methanol conversion
DME
Coke deposition

ABSTRACT

The FER-type zeolite was found to be a reliable catalyst for DME synthesis via both direct CO_2 hydrogenation or gas phase methanol dehydration. In this work, the effect of the crystal size of FER-type zeolites on the catalytic behavior during methanol-to-DME conversion is studied. A series of FER-type crystals ranging from 0.1 μm to 10 μm in size were synthesized and their physicochemical properties (e.g. crystal morphology, acidity, textural characteristics) analyzed. The catalytic performance of FER-type catalysts was studied in a wide range of reaction temperatures (120–280 °C). The set experimental data show that the catalytic effectiveness of FER-type catalysts in terms of methanol conversion, DME selectivity and coke resistance, can strongly be improved by reducing the zeolite crystal size.

1. Introduction

Zeolites are crystalline microporous aluminosilicates whose catalytic properties are largely explored for decades. The ever-growing success of zeolites as industrial catalysts is mainly resulting from their unique molecular shape-selectivity, owing to a well-defined regular microporous structure, combined with tunable active sites. Generally, both Brønsted and Lewis type acid sites are simultaneously present in a zeolite and their concentration, distribution, strength and location affect the overall activity, product selectivity and deactivation of the catalyst [1]. Unfortunately, the exceptional shape selectivity of zeolites is coupled with severe intracrystalline mass transfer limitations due to comparable size of the diffusing molecules and the zeolite channels. The interaction between diffusing molecules and channel walls, known as configurational diffusion, hinders the reaction rate and reduces the catalyst efficiency. In order to overcome this problem, one of the strategies to be adopted in order to reduce mass transfer limitation is to synthesise zeolites with a secondary pore system of larger channels [2]. In this class of materials, known as hierarchical or mesoporous zeolites, intrinsic micropores are connected with a mesoporous channel net, promoting the diffusion to/from the active sites. During the last decade, several methods have been developed for hierarchical zeolites preparation, using bottom-up or top-down approaches [2–4]. Depending on the adopted procedure, pore architecture, position and topology of mesopores of zeolites can be varied and thus their catalytic performances [5,6].

The reduction of the crystal size to nanometric scale is another option largely explored in order to reduce the diffusion path length and thus to increase catalyst effectiveness [8,9]. Yang et *al* [10]. showed that the crystal size strongly affects both product distribution and catalyst deactivation, during methanol (MeOH) conversion to olefins over SAPO-34 catalysts (CHA-type structure). Namely, the utilization of nano-sized SAPO-34 remarkably enhanced the olefins yield and catalyst life time and the positive effect of nano-zeolites in methanol-to-olefin conversion was also reported by other authors [11–15]. The superiority of nano-sized zeolite in catalysis has also been demonstrated for other zeolite-catalysed reactions such as *n*-hexane cracking [16], hydrocracking of heavy vacuum gas oil [17,18], Fischer-Tropsch process [19], alkane and xylene isomerization [20,21], biomass pyrolysis [22], ethanol to propylene [23] and others [24].

Nano-sized zeolite crystals can be obtained via a careful optimization of the synthesis gel composition and crystallization conditions, as summarized by Mintova et al. [25,26] and Di Renzo [27]. One key factor is the ability to induce simultaneous nucleation events,

* Corresponding author at: Department of Environmental and Chemical Engineering, University of Calabria, Via P. Bucci, I-87036, Rende, CS, Italy.
** Corresponding author at: Normandie Univ., ENSICAEN, UNICAEN, CNRS, Laboratoire Catalyse et Spectrochimie, 14000, Caen, France.
E-mail addresses: enrico.catizzone@unical.it (E. Catizzone), valentin.valtchev@ensicaen.fr (V. Valtchev).

https://doi.org/10.1016/j.apcatb.2018.10.060
Received 23 July 2018; Received in revised form 19 October 2018; Accepted 24 October 2018
Available online 28 October 2018
0926-3373/

producing a zeolite with narrow particle size distribution. Such conditions were achieved for several industrial relevant zeolites by fine control of the reaction parameters (e.g. gel composition, alkalinity, dilution, temperature, gel aging, etc.) [7,25–32].

Recently, the crystallization of zeolites in the presence of a surfactant was reported as an unconventional method to prepare nano-sized MFI and MOR crystals [33–35]. Different surfactants, anionic, cationic or non-ionic molecule, can be employed.

SLS was proposed as an emulsifier to obtain highly crystalline nano-sized FER crystals in the range 200–400 nm when piperidine is used as a structure directing agent. CTABr or Span 60 will lead to the formation of an amorphous phase and 1–3 μm large ferrierite crystals, respectively [36].

Recent works showed that the FER-type zeolite is promising acid catalyst to produce dimethyl ether (DME) via both methanol dehydration [37–39] and one-pot CO_2 hydrogenation [40–42]. DME has a bright future ahead as a reliable alternative fuel for diesel engines due to its high cetane number and soot-free emissions [43]. Moreover, DME can also be an intermediate in the olefins and fine chemicals production, and it is considered as a reliable energetic vector to introduce renewable energy in the chemical industry [44,45], since it can be produced from biomass or CO_2.

Compared with other zeolite catalysts (e.g. beta, MFI, MOR, MTW, EU-1), the ferrierite shows a higher DME selectivity and resistance to deactivation by coke deposition [38,42]. The effect of acidity of the FER-type zeolite on methanol dehydration to DME reaction was also investigated revealing that a higher Lewis acid concentration will increase the catalyst effectiveness [46]. The beneficial use of nano-sized zeolites in methanol dehydration to dimethyl ether reaction was recently investigated by Rownaghi et al. [47] using ZSM-5 zeolites. The authors showed that by reducing the crystal size from 1.2 μm to 0.12 μm, both the DME selectivity and the MeOH conversion improved significantly.

According to that, the aim of this study is to investigate the behaviour of nanosized FER-zeolites in DME synthesis. The crystals size was varied from nano- to micron-sized dimension and the impact of crystals size on the number and distribution of active sites was studied in vapour phase methanol dehydration.

2. Experimental

2.1. Samples preparation

All FER-type zeolite samples were prepared by using pyrrolidine (Py, Aldrich) as structure directing agent (SDA) adopting the synthesis procedure described elsewhere [29] and using a gel with the following molar composition:

Py – 1.6 Na_2O – Al_2O_3 – 20 SiO_2 – 400 H_2O

The used chemicals were: Colloidal silica Ludox AS-40 (SiO_2, 40 wt % suspension in water, Aldrich), sodium aluminate ($NaAlO_2$, Aldrich), sodium hydroxide (Aldrich) and distilled water.

All the syntheses were carried out in 60 ml PTFE-lined stainless steel autoclaves using a tumbling oven (tumbling speed = 20 rpm). The crystallization of micron-sized FER-type zeolite (named M-FER) was carried out at 180 °C for 120 h. With the aim to reduce the crystal size, sodium lauryl sulfate (SLS, Aldrich) was used as a surfactant in the sampled labelled as NP-FER. A SLS/Al_2O_3 molar ratio equals to 0.3 was used and crystallization was carried out at 180 °C for 75 h.

The effect of seeds was also evaluated by adding 3 wt. % seeds (H-form NP-FER) with respect to silica in the above reported synthesis gel. Crystallization of this system was performed at 160 °C for 60 h and before synthesis, the gel was aged at 80 °C for 48 h under stirring condition (stirring rate: 500 rpm). The solid synthesized following this from this procedure is reported as NC-FER.

As standard procedure, after synthesis, the solid was recovered by suction filtration and washed several times with distilled water. Organic SDA was removed by calcination in air at 550 °C for 8 h. After this treatment, the H-form of the synthesized zeolites was prepared by an ion-exchange with NH_4Cl solution [37], followed by calcination in air (550 °C for 8 h).

2.2. Physicochemical characterization

Powered X-ray diffraction patterns of synthesised samples were obtained with APD 2000 Pro GNR instrument (Cu Kα radiation, λ = 1.5406, 40 kV, 30 mA, 5-50° 2θ range, scanning step 0.2°·s^{-1}). The crystal size and shape were studied using a scanning electron microscope (FEI model Inspect). Nitrogen adsorption/desorption isotherms were carry out on H-form samples at 77 K with a Micromeritics ASAP 2020. The specific surface area was calculated using the BET equation, whilst the micropore volume and external surface were estimated by the *t*-plot method. Thermogravimetric analysis (TG/DTA) was carried out in air on a DTG-60 Shimadzu instrument in the range 25 °C–850 °C (heating rate: 5 °C min^{-1}). The chemical composition of the samples was determined via atomic absorption spectroscopy (GBC 932). ^{27}Al-NMR spectra of H-form samples were acquired on a Bruker Advance 500 MHz spectrometer [48].

The *in-situ* FT-IR technique was used to study the surface acidity of the samples. FTIR measurements were carried out on a Nicolet Magna 550-FTIR spectrometer at 4 cm^{-1} optical resolution with a DTGS detector. Samples to be analysed were pressed as self-supported wafers (diameter 13 mm, 18 mg). Before the spectrum acquisition at room temperature, each sample was pre-treated in the IR cell connected to the vacuum line at 393 K (1 K/min) for 4 h and at 723 K (1 K/min) for 5 h under 10^{-6} torr. Deuterated acetonitrile (CD_3CN) was used as a probe to estimate total acidity and Brønsted/Lewis distribution as this base molecule is able to diffuse in both 8- and 10-membered rings of FER structure. 2,6-dimethyl pyridine and *tert*-butyl nitrile were used as probe molecules to estimate the number of Brønsted and Lewis acid sites located on the external crystal surface. Probe molecules were adsorbed at room temperature (295 K) with a saturation pressure of 0.5 torr.

2.3. Catalytic tests

Vapor-phase methanol dehydration reaction was carried out in a lab-scale apparatus, using a quartz tubular reactor [49]. A mixture of methanol/nitrogen (methanol content 0.06 mol/mol) was fed to the reactor containing 70 mg of catalyst (pellets form 300–500 μm) with a total flow rate of 60 Nml·min^{-1}. Catalytic tests were carried out in the 120–280 °C range under atmospheric pressure. Stability tests were performed at 280 °C for a duration up to 60 h. Reactor out-stream composition was analyzed by an on-line gas-chromatograph equipped with flame ionization detector [49].

2.4. Coke analysis

The amount of carbonaceous solid (named coke) deposited during time-on-stream tests at 280 °C was determined via thermogravimetric analysis of exhausted samples [37]. The composition of coke was measured via GC–MS analysis following a dissolving/extracting procedure [38]. The morphology and distribution of coke on zeolite surface was also investigated by Field Emission Gun Electron Scanning Microscopy LEO 1525 ZIESS, after metallization with Cr and elemental composition was determined using a Bruker Quantax EDS.

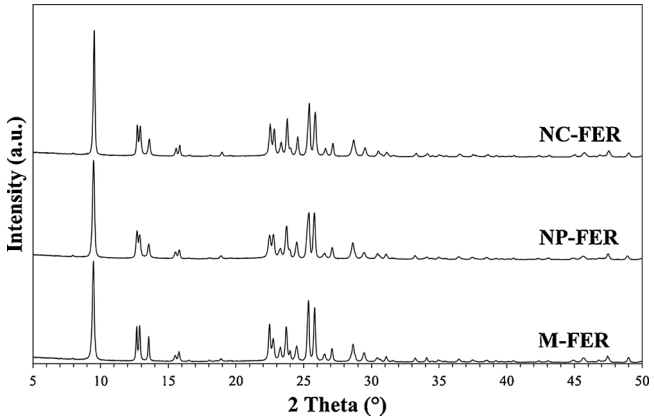

Fig. 1. XRD patterns of studied samples.

3. Results and discussion

3.1. Physicochemical properties of investigated samples

XRD analysis showed that all samples are highly crystalline FER-type materials, neither other phases nor amorphous material was identified (Fig. 1). SEM images of M-FER, NP-FER and NC-FER are shown in Fig. 2(A)–(C), respectively. M-FER shows stacked plate-like crystals with a well-developed {1 0 0} face with following dimensions: length 8–12 μm, length/width ratio around 2 μm and thickness 0.1 μm (Fig. 2A). The use of SLS surfactant resulted in the formation of non-stacked plate-like crystals with size ranging between 300 and 500 nm (Fig. 2B). The addition of seeds allowed to decrease the crystal size to about 100 nm (Fig. 2C). Chemical analysis data reported in Table 1 show that the samples exhibit a similar bulk aluminium content (AC), but a higher aluminium content on the surface (AS) was found, with major evidence for smaller crystals. The analysis of the local structure by ^{27}Al MAS NMR is presented in Figure S.1 (Supplementary Information), revealing that both, tetrahedral and octahedral aluminium species, are present in the investigated samples, with a chemical shift of about 54 ppm and 0 ppm, respectively. The relative concentration of octahedral aluminium increases as the crystal size decreases from ca. 14% of the largest crystals to ca. 21% for the smallest ones (Table 1). The higher AS in the nanocrystals is obviously related to the presence of extra-framework aluminium on their outer surface.

The N_2 adsorption/desorption isotherms at 77 K presented in Fig. 3 reveal some differences in the porosity and the texture of the investigated samples. M-FER exhibits a type-I isotherm, where a second uptake is observed at 0.7-0.8 relative pressure with hysteresis. in the later is a consequence of stacking of platelets of about 100 nm thickness [50,51]. NP-FER exhibits a less evident hysteresis loop probably due to limited agglomeration between the particles [52]. On the contrary, NC-FER exhibit a type-H4 hysteresis loop at lower relative pressure (starting from about 0.4) typical of agglomerates of particles forming mesopores with uniform size and shape [51–54]. As reported in Table 1 both BET surface area and micropore volume are typical of highly crystalline FER-type materials [29]. The differences in micropore volume could be related to the presence of extra-framework aluminium species inside the pores, since samples with a higher concentration of extra-framework aluminium species exhibit lower micropore volume. The analysis of the local structure of aluminium by ^{27}Al MAS NMR is presented in Figure S.1 (Supplementary Information), revealing that both, tetrahedral and octahedral aluminium species, are present in the investigated samples, with a chemical shift of about 54 ppm and 0 ppm, respectively. The relative concentration of octahedral aluminium increases as the crystal size decreases from ca. 14% of the largest crystals to ca. 21% for the smallest ones (Table 1).

Fig. 4(A) shows the FT-IR spectra of investigated FER-type samples

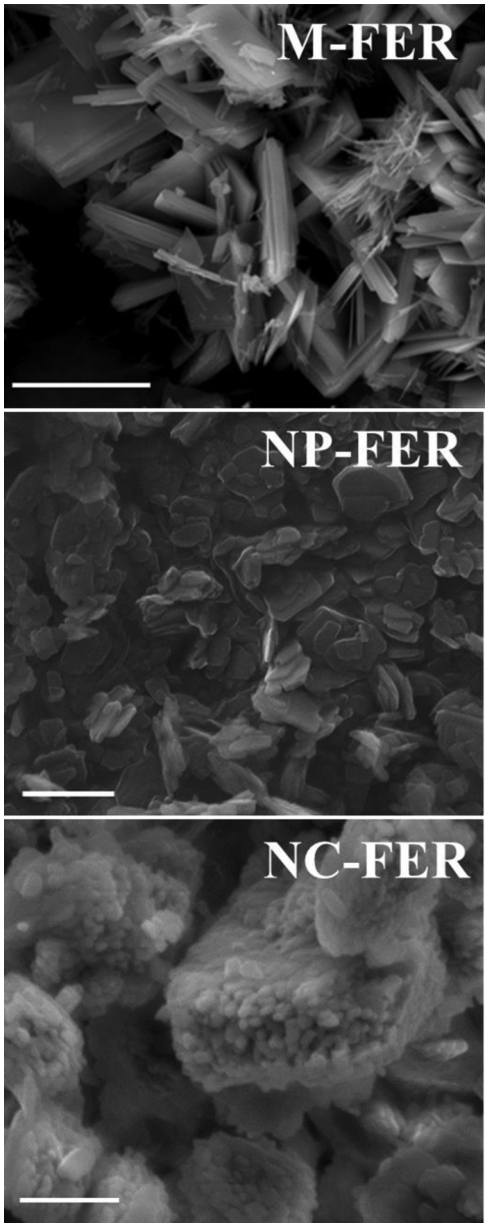

Fig. 2. SEM images of studied samples.

Table 1
Physicochemical characteristics of the series of studied zeolite samples.

Sample	Average crystal size (μm)	Al/(Si + Al) (mol%)		AS/AC ratio	Al_{EF}[c] (%)	S_{BET}[d] (m^2/g)	V_{mic}[e] (m^2/g)
		In crystal (AC)[a]	On surface (AS)[b]				
M-FER	5-10	9.6	11.4	1.2	14	332	0.134
NP-FER	0.3-0.5	10.4	13.0	1.3	17	314	0.125
NC-FER	0.1	9.4	13.3	1.4	21	304	0.122

[a] Determined by AA.
[b] Determined by EDX.
[c] Percentage of aluminium in octahedral coordination estimated via 27Al-NMR.
[d] BET surface area.
[e] Micropore volume calculated by t-plot method.

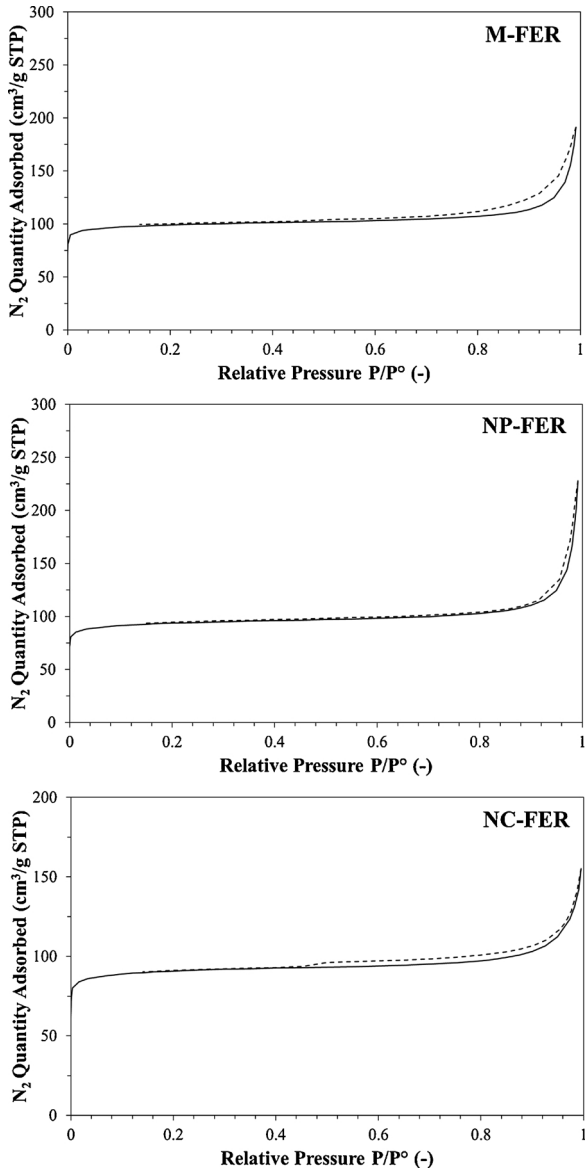

Fig. 3. Nitrogen adsorption/desorption isotherms of studied samples.

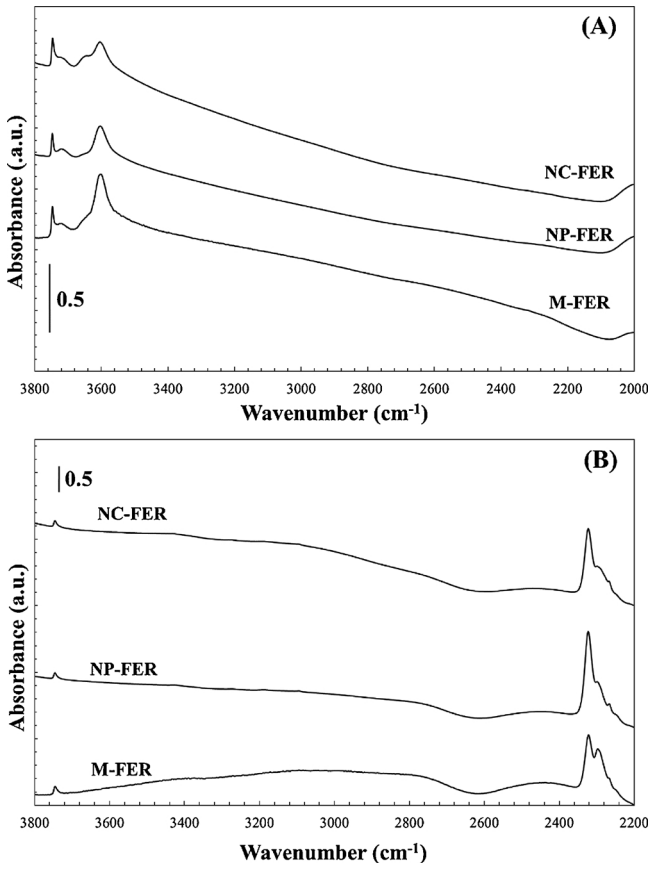

Fig. 4. FT-IR spectra of studied samples after evacuation at 723 K for 4 h (A) and after adsorption of D_3-acetonitrile at room temperature (B).

prior to the adsorption of the probe molecule. The sharp band at 3746 cm^{-1} is associated with terminal silanol groups located on the external surface. The shoulder at 3720-3730 cm^{-1} originates from silanols located inside the pores. The band at 3600 cm^{-1} is characteristic of bridging Si(OH)Al Brønsted sites. The broad shoulder around 3650 cm^{-1} is typically related to highly distorted or extra-framework aluminium species that can act as Lewis acid sites [55–59]. Spectra reported in Fig. 4 reveal that all the samples show similar bands in the 3720-3746 cm^{-1} region, suggesting similar concentration and location of silanol groups. On the contrary, FT-IR spectra differ in the 3600-3680 cm^{-1} region: the band height at 3600 cm^{-1} follows the order M-FER > NP-FER > NC-FER suggesting that M-FER possess a higher concentration of bridging Si(OH)Al Brønsted sites than the other samples. NC-FER contains a more pronounced band at 3630-3680 cm^{-1} region showing a higher concentration of extra-framework aluminium species for nanosized sample, in agreement with the ^{27}Al MAS NMR data.

In order to better discriminate between Lewis and Brønsted acid sites, in the 3600-3680 cm^{-1} region the bands entirely disappear after the adsorption of CD_3CN, indicating that the acid sites of investigated samples are fully saturated (Fig. 4(B). A small number of terminal silanols are still present after CD_3CN adsorption, confirming the low-acidic character of these groups, whilst internal silanols (bands at around 3725 cm-1) totally disappear.

Spectra analysis suggests that d_3-acetonitrle exhibits at least five stretching modes of ν(C≡N) in the region 2220–2360 cm-1 as reported in Figure S.2. IR band at about 230 cm^{-1} is ascribed to coordinatively bonded CD_3CN on electron acceptor aluminium sites that act as Lewis centres whereas the band at 2296-2298 cm^{-1} derives from coordination of probe molecule with bridging OH groups that act as Brønsted acid sites. The presence of a ν(C≡N) stretching band at 2275-2280 cm^{-1} is associated to the interaction of CD_3CN with zeolite defects (i.e., silanols) whereas the presence of physisorbed and liquid phase CD_3CN is characterized by the bands at 2265 cm^{-1} and 2250 cm^{-1}, respectively [60,61]. The number of bridging Brønsted sites was calculated from the area of the band observed at 2296 cm^{-1} by adopting an extinction coefficient of 2.05 cm/μmol, whilst the number of Lewis acid sites was calculated from the area of the band centered at 2322 cm^{-1} by adopting an extinction factor of 3.6 cm/μmol [60].

In order to probe the external surface of ferrierite crystals two bulky molecules, 2,6-dimethyl pyridine (lutidine) and tert-butylnitrile (pivalonitrile), were employed. The difference spectra after saturation with lutidine are presented in Fig. 5(A). Besides the bands characteristic of lutidine, a negative signal due to the consumption of silanols is observed at 3747 cm^{-1}. This result shows that the majority of silanols are situated at the external surface of ferrierite, which is in agreement with the data reported by van Donk et al. [62]. The relative magnitude of the signal at 3600 cm^{-1}, representing the consumption of Brønsted acid sites, points out that only a small percentage of the total Brønsted acid sites is consumed by lutidine. By analysing the spectra in the 1700-1500 cm^{-1} range both bands specific for lutidine:Lewis at 1580-

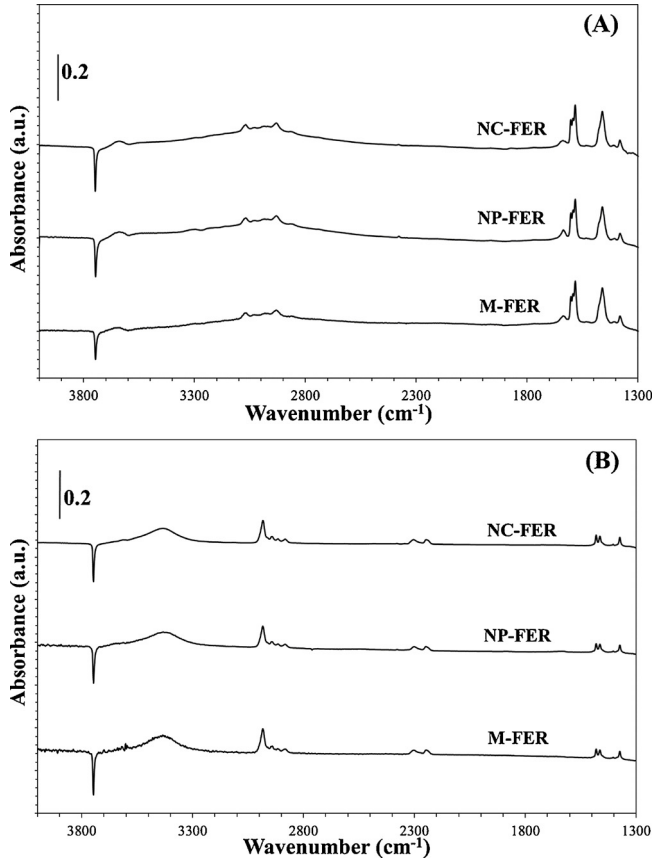

Fig. 5. Difference FT-IR spectra of studied samples after saturation with 2,6-dimethyl pyridine (A) or tert-butylnitrile (B).

1603 cm^{-1} and lutidine:Brønsted at 1630-1650 cm^{-1} appear. As reported elsewhere [63,64] lutidine is strongly adsorbed on Brønsted even after outgassing at high temperature whilst readily desorbs from the Lewis sites because of limited interaction by steric hindrance. For this reason, lutidine is considered a suitable probe molecule to estimate Brønsted sites [64,65]. The Brønsted acid sites on the external surface were estimated by the band at 1630-1650 cm^{-1} using the molar extinction coefficient reported by Onfroy et al. [66]. In order to quantify external Lewis acidity probing with tert-butylnitrile was employed. On the other hand, due to overlapping signals, quantification of the Brønsted acidity by tert-butylnitrile molecule is hindered. Based on the literature data both, the molar extinction coefficient and the identification of different bands, was performed [67,68]. As reported in Fig. 5(B), the coordination between the probe molecule on a Lewis site is found at 2305 cm^{-1}. Although a high percentage of Lewis acidity is observed in all three samples, no surface enrichment is detected.

The quantification of acid sites resulted from FT-IR analysis is summarized in Table 2. NP-FER sample shows the highest Lewis acid

Table 2
Acidic properties of the series of studied samples.

SAMPLE	Total acidity[a] (μmol/g)		External acidity (μmol/g)	
	Brønsted	Lewis	2,6-DMP[b]	TBN[c]
M-FER	598	489	15	12
NP-FER	363	948	12	13
NC-FER	276	521	8	10

[a] Determined by FT-IR after adsorption of d_3-acetonitrile.
[b] Determined by FT-IR after adsorption of 2,6-dimethyl pyridine.
[c] Determined by FT-IR after adsorption of tert-butylnitrile.

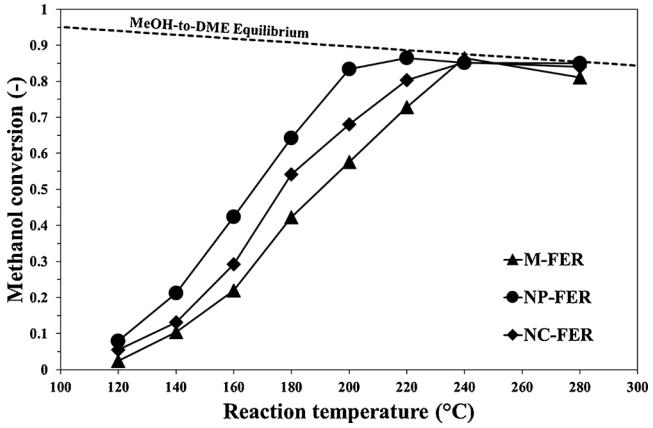

Fig. 6. Methanol conversion as a function of reaction temperature.

sites concentration followed by NC-FER and M-FER. On the contrary, the highest bridging Brønsted acid sites concentration is measured for M-FER followed by NP-FER and NC-FER. Note that the investigated samples possess a similar aluminium content. Therefore, the set of data points out that the smaller crystals contain less Brønsted sites than larger ones. We relate this result with the synthesis conditions used to obtain nanocrystals that might cause a lower aluminium incorporation [69]. Although NC-FER exhibits the highest aluminium content on the external surface, the lower amount of external acid sites was found on this sample, indicating that not all the external aluminium species possess acidity properties [69].

For all the samples, less than 2% of total acid sites are located on the external surface of zeolite crystals suggesting that the majority of acid sites, either Brønsted- or Lewis-type, are mainly located in the pore volume. The latter result permits to assume that the effect of the external surface acidity is negligible in comparison with the internal acidity on catalytic behaviour of investigated zeolites.

3.2. The effect of crystal size on catalytic activity

The methanol conversion is reported in Fig. 6 in the reaction temperature range 120 °C–280 °C. The following activity order NP-FER > NC-FER > M-FER can be observed up to 220 °C whilst all catalysts exhibit a similar conversion, close to the equilibrium thermodynamic value, at high temperatures. Since the observed differences in catalytic activity can be related to both acidity and crystal size, a turnover frequency (TOF) analysis was employed to shed more light in the catalytic reaction. Both intrinsic reaction rate and an accurate counting of active sites are necessary in order to estimate a TOF value. It is well-known that only an apparent reaction rate can be calculated when zeolites are used as catalyst due to severe intracrystalline mass transfer limitation; furthermore, both Brønsted and Lewis acid sites catalyse dehydration of methanol to DME, even if Lewis acid sites show a higher activity [46,70]. Therefore, in this work, an apparent turnover frequency (TOF_{app}) value is calculated by considering the observable methanol conversion rate and both Brønsted and Lewis acid sites number calculated from FT-IR analysis. Silanols sites were not included since they are not active towards such reaction under the investigated conditions. TOF_{app} is calculated by the following equation:

$$TOF_{app} = \frac{n^0_{nMeOH} \cdot x_{MeOH}}{B + L}$$

with n^0_{nMeOH} the inlet methanol flow rate (e.g. expressed in μmol/h), x_{MeOH} the methanol conversion grade (dimensionless) and B and L are Brønsted and Lewis acid sites number, respectively. The apparent TOF analysis was performed with conversion data at 180 °C [38] and the estimated values are reported in Table 3. The obtain values showa positive effect of reducing crystal size on the efficiency of the catalyst in

Table 3
Apparent turnover frequency at 180 °C, DME selectivity at 240 °C and 280 °C, and by-products distribution at 280 °C.

SAMPLE	TOF_{app} at 180 °C (h^{-1})	DME Selectivity (%)		By-products loop distribution at 280 °C (%)		
		240 °C	280 °C	Methane	Ethene	Propene
M-FER	49	96	90	0.35	0.16	0.49
NP-FER	62	98	95	0.46	0.18	0.36
NC-FER	86	100	99	N.D.	N.D.	N.D.

terms of apparent turnover rate since TOF_{app} increases from 45 h^{-1} to 65 h^{-1} by decreasing the crystal size from micro- to nano-metric scale. A recent work reports that Lewis acid sites exhibit higher activity than Brønsted acid sites during methanol to DME reaction leading to higher TOF value for FER-type zeolites with higher Lewis acid sites concentration [46]. The results obtained in this work report that, although NC-FER possesses a LAS concentration much lower than NP-FER, it exhibits a higher apparent TOF indicating that the control of mass transfer limitation in zeolites plays a crucial role in Methanol-to-DME reaction.

For reaction temperatures up to 220 °C, DME was detected in the reactor out-stream, in agreement with previous studies [37–39]. At 240 °C, traces of hydrocarbons, mainly methane, ethylene and propylene are formed, causing a DME selectivity drop; which is more critical for larger crystals while no by-products were detected when NC-FER was tested (see Table 3).

By increasing the reaction temperature to 280 °C, DME selectivity decreases to 95% and 90% for NP-FER and M-FER, respectively.The DME selectivityis about 99% for NC-FER. For both, NP-FER and M-FER, by-products were quantified from GC analysis whilst similar analysis was not possible for NC-FER because of too low signals. Methane, ethene and propene were mainly formed as by-products. In particular, the distribution of by-products loop is reported in Table 3. The results clearly show that the ethene fraction is similar in M-FER and NP-FER samples whilst the yield of methane was higher on the NP-FER sample, probably related to its higher Lewis acid sites concentration [46].

It is known that the formation of hydrocarbons from methanol, involves a complex mechanism (such as hydrocarbon pool in the case of olefins) where methanol might be dehydrated to DME and then both DME and methanol are converted to hydrocarbons [71–75]. The obtained selectivity results suggest that in case of nano-sized crystals it is possible to reduce the residence time inside the crystal and, as a consequence, formed DME is able to effectively diffuse outside the crystal reducing the occurrence of consecutive reactions [13,75]. On the contrary, on large crystals (e.g. M-FER), more side reactions can occur. Time-On-Stream tests carried out at 280 °C showed that all catalysts keep a nearly constant methanol conversion grade for 60 h (Figure S.3, Supporting Information). Smaller crystal (NP-FER and NC-FER) showed stable DME selectivity up to 60 h. The selectivity of micron-sized crystals (M-FER) increased from 0.90 to 0.98 after 60 h.

3.3. Coke analysis

The amount of coke deposited on the investigated catalysts during methanol dehydration at 280 °C monitored via Thermogravimetric/Differential Thermal Analysis (TG/DTA) is presented in Fig. 7. It clearly appears how the coke deposition is favourably affected by the increase in crystal size: the measured amount of deposited coke is 75 mg_{coke}/g_{cat}, 69 mg_{coke}/g_{cat} and 46 mg_{coke}/g_{cat} for M-FER, NP-FER and NC-FER, respectively, after 60 h of Time-on-Stream.

In order to obtain quantitative information on the coke formation rate, the experimental data was fitted to a first order model [37]:

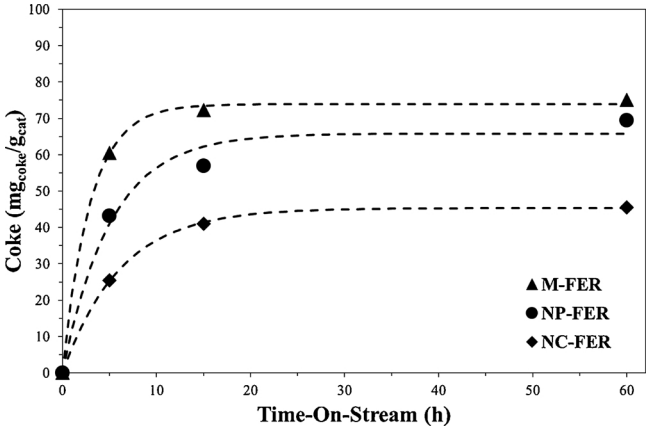

Fig. 7. Coke content in zeolite catalysts deposited at 240 °C as a function of TOS.

$$C = C_{\infty}\cdot\left(1 - e^{-t/\tau}\right) \quad (1)$$

where C is the specific coke amount (mg_{coke}/g_{cat}), C_{∞} the plateau value and τ the characteristic time (h). From this equation, the initial coke deposition rate r_0 ($mg_{coke}/(g_{cat}\cdot h)$) can be estimated as:

$$r_0 = \left.\frac{dC}{dt}\right|_{t=0} = \frac{C_{\infty}}{\tau} \quad (2)$$

The experimental data were fitted via a nonlinear regression by using a commercial software (Curve Expert Professional 2.0) and the model parameters values are summarized in Table 4. The calculated kinetic parameters suggest that the crystal size strongly affects the kinetics of coke formation, in terms of either carbon amount or deposition rate. In fact, by decreasing the crystal size both C_{∞} and r_0 are reduced as a consequence of the utilization of nanosized zeolite in methanol-to-DME dehydration.

In order to establish the composition of the deposited carbon, a coke extraction procedure was carried out following the method developed by Guisnet and Magnoux [76]. No insoluble carbon particles were observed, suggesting that all the carbonaceous deposits can be referred to "soluble coke" which can be analyzed via GC–MS technique. Fig. 8 reports the GC–MS spectra for the extracted carbonaceous deposits for the samples after 5 h, 15 h and 60 h of reaction. This analysis revealed that no polyaromatics were detected and the coke-forming compounds are poly-substituted benzenes with a grade of substitution depending on reaction time and crystal size. Over the micron-sized ferrierite crystal (M-FER), the coke is manly composed from di-methyl benzene (Di-MB) and tetra-methyl benzene (Tetra-MB) with traces of hexa-methyl benzene (Hexa-MB). The same identity of coke molecules are detected for NC-FER, whereas NP-FER only forms Tetra-MB.

Di- and Tetra-MB can be accommodated in ferrierite cages, whilst bulkier molecules, such as Hexa-MB, are most probably formed on the external surface [77,78]. The formation of Hexa-MB on the NC-FER sample might be related to the crystal morphology of this sample. The clustering of nano-crystals may induce inter-crystalline mass transfer limitations, higher retention time, and thus increase the probability of a transformation of precursors molecules into Hexa-MB. Hexa-MB is also

Table 4
Coke formation: kinetic parameters for 1st order model.

SAMPLE	C_{∞} (mg_{coke}/g_{cat})	τ (h)3	r_0 ($mg_{coke}/g_{cat}\cdot h$)	r^2 (—)
M-FER	73.9 ± 0.9	2.9 ± 0.2	25.5 ± 0.5	0.999
NP-FER	65.8 ± 0.4	5.1 ± 1.2	12.9 ± 2.0	0.983
NC-FER	45.3 ± 0.3	6.1 ± 0.1	7.4 ± 0.1	0.999

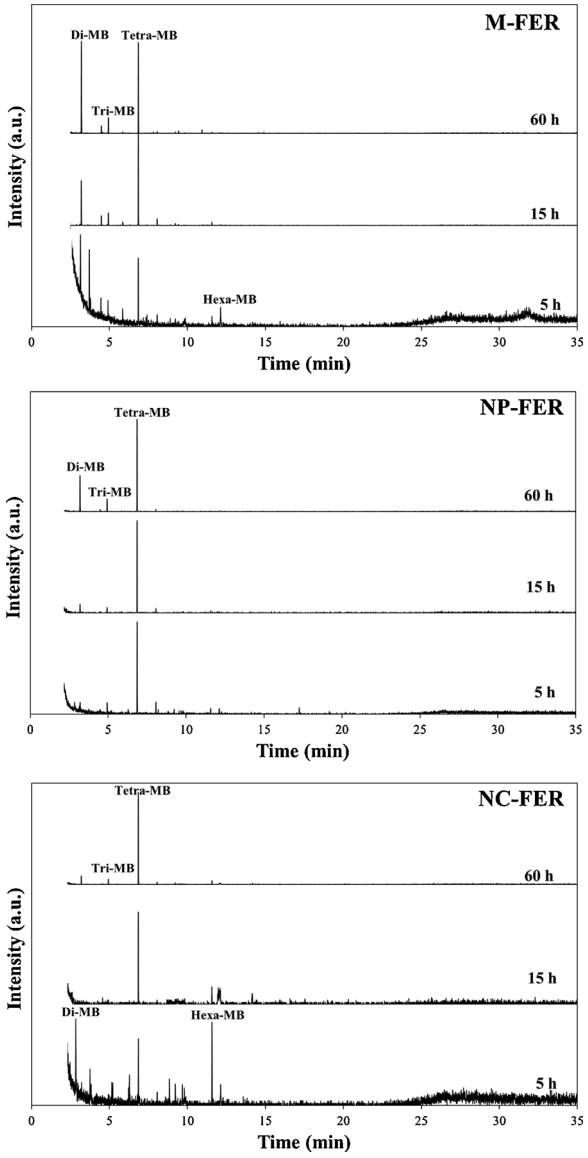

Fig. 8. GC–MS spectra of carbonaceous deposit extracted from soluble coke of studied samples after 5 h, 15 h and 60 h reaction at 240 °C.

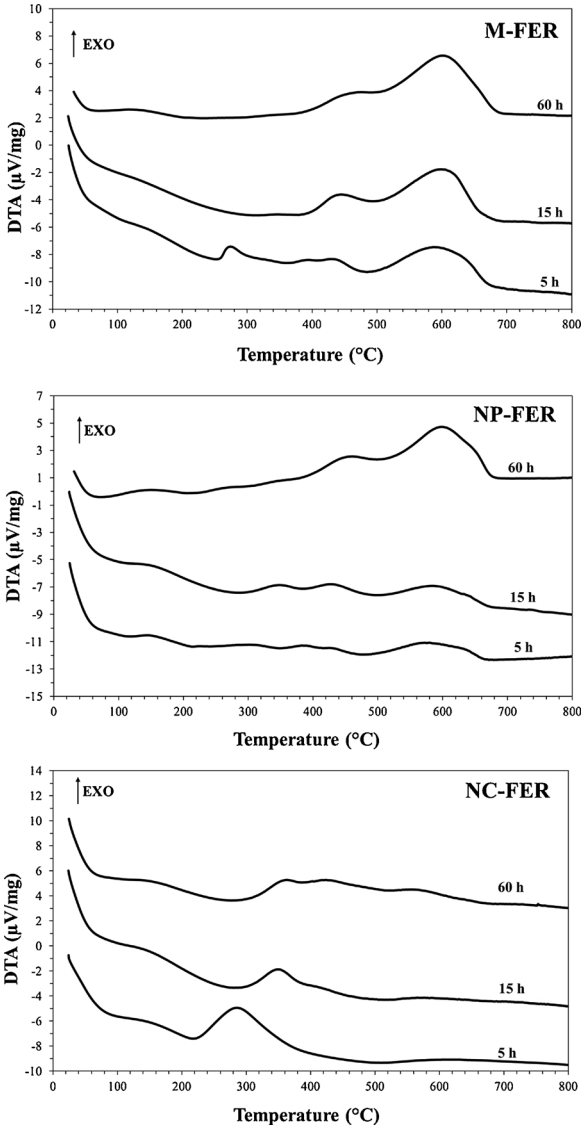

Fig. 9. DTA profiles ofstudied samples after 5 h, 15 h and 60 h reaction at 240 °C.

detected in M-FER, where stacking along the pinacoidal plane is largely observed. In contrast the small single crystals of the NP-FER sample ensure a fast release of coke precursors from the crystal surface. Consequently no Hexa-MB is observed. As the reaction time increases, Tetra-MB becomes the main observed carbonaceous species for NP-FER, while larger M-FER and NP-FER crystals contain tetra-MB and di-MB molecules.

Fig. 9 presents the DTA profiles for the series of catalysts after 5 h, 15 h and 60 h reaction at 240 °C. The exothermic peaks are related to the combustion of carbonaceous species, revealing that this effect occurs at different temperatures and depends on both, the reaction time and crystal size.

This is in agreement with the earlier discussed GC–MS analysis as, when Hexa-MB is present, which is the case after 5 h of reaction for NC-FER and M-FER samples, a combustion peak is present at a relatively low temperature (i.e. 285 °C and 274 °C, respectively). This peak can then be associated with the combustion of Hexa-MB located on the external surface of the crystals. In fact, when Hexa-MB is absent, the combustion phenomena take place at a higher temperature and it can be attributed to the thermal degradation of Di- or Tetra-MB molecules trapped within the micropores. On the other hand, if Tetra-MB is the only present specie, as in the case of NP-FER after 15 h reaction, the exothermic peaks appear at ca. 344 °C, 435 °C and 590 °C suggesting different locations and force of interaction between the molecule and FER framework. On the basis of DTA profiles, the carbon deposit can be

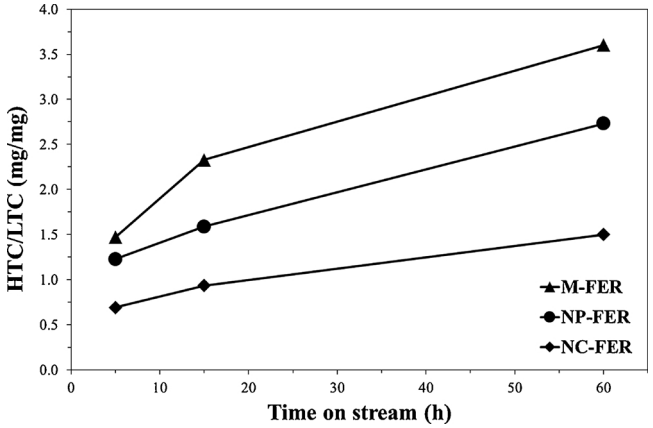

Fig. 10. HTC/LTC ratio as a function of reaction time.

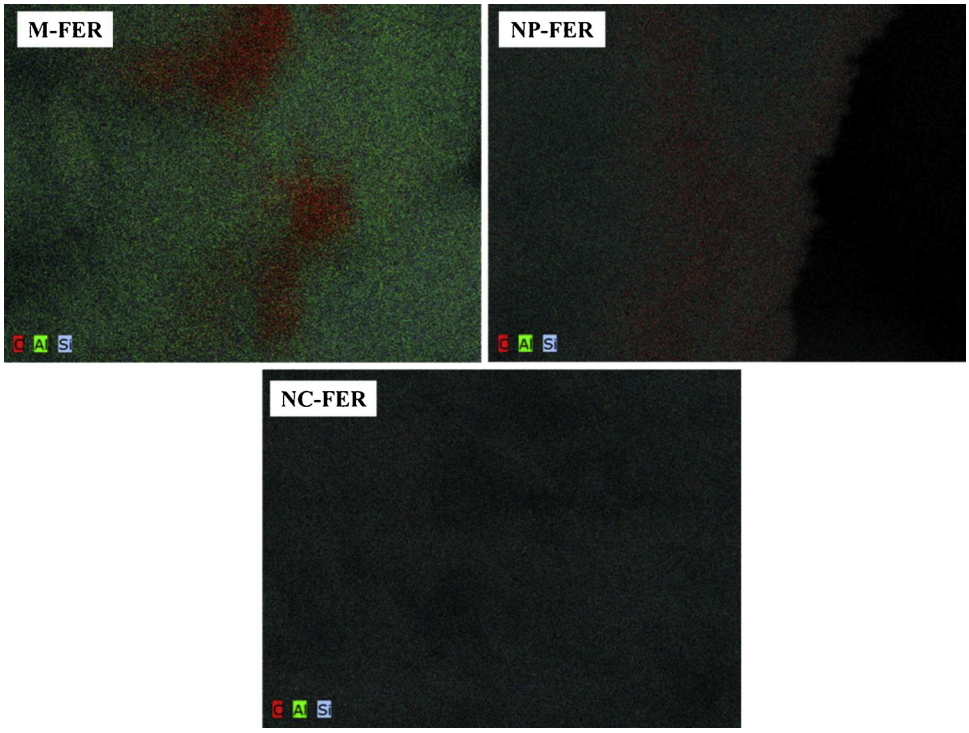

Fig. 11. EDX mapping images of studied samples after 60 h reaction at 240 °C.

classified as low temperature coke (LTC) and high temperature coke (HTC) associated to carbon deposit burning below or above 500 °C, respectively. According to this classification, it is possible to calculate the amount of LTC and HTC from thermogravimetric analysis and assess the effect of reaction time on HTC/LTC. Fig. 10 shows that HTC/LTC ratio increases as a function of reaction time in the following order M-FER > NP-FER > NC-FER. The data unambiguously show that the decrease of crystal size leads to reduction of HTC. Consequently, the deposited carbon can be eliminated by using milder regeneration conditions. In order to gain a better understanding of the location of the carbonaceous species, SEM-EDX analysis was performed (Fig. 11). The EDX mapping clearly reveals that the external coke is homogenously distributed on NC-FER crystals while large carbonaceous agglomerates form on zeolites with larger crystals. This data also confirm that the zeolite crystal size/morphology play a fundamental role in coke deposition in terms of amount, composition and distribution.

4. Conclusions

The vapour-phase dehydration of methanol to dimethyl ether on FER-type zeolite crystals was studied. The set of experimental data show that the decrease of crystal size from 5 to 10 μm to 100 nm leads to an increase of methanol apparent turnover frequency due to reduced intracrystalline mass transfer limitation and improved acid sites accessibility. At 240 °C DME selectivity increases from 0.96 to 0.98 by reducing the crystal size from 5 to 10 μm to 300–500 nm whereas no by-products were detected for smaller nano crystals., By-products distribution analysis indicated that methane is preferably formed foron catalysts with higher Lewis sites concentration. The thorough assessment of the carbon deposition process revealed that: (i) The coke consists of polymethyl benzene (PMB) molecules whose composition depends on both the zeolite crystal morphology and the reaction time. The formation of Hexa-MB is observed during the first 5 h for samples with intracrystalline voids, while only Di-MB and Tetra-MB are observed for longer reaction time. The relative Di-MB/Tetra-MB ratio decreases with the reduction of crystal size. Furthermore, (ii) the coke deposition can be reduced and slowed down in rate by using zeolites with smaller crystals and (iii) the regeneration of nano-sized zeolite catalysts can be performed at a lower temperature. As a general conclusion, this work showed that the nano-sized FER-type crystals are a much more efficient catalyst in methanol dehydration to DME with respect to their micron-sized counterparts.

Authors' contributions

Enrico Catizzone: manuscript preparation; XRD and porosimetric analysis, TG/DTA; manager of experimental part.

Stijn van Daele: manuscript preparation and revision; characterization of materials by FT-IR analysis.

Massimo Migliori: manuscript preparation and revision; manager of experimental part.

Micaela Bianco: synthesis of materials and catalytic tests.

Alessandro Di Michele: characterization of exhausted catalysts.

Alfredo Aloise: Chemical and Physical analysis.

Valentin Valtchev: Research plan discussion and revision of the manuscript.

Girolamo Giordano: revision of the manuscript; manager of the research project.

Acknowledgments

The authors gratefully acknowledge Dr. Pietro Argurio (University of Calabria) for chemical analysis via atomic absorption spectroscopy and Dr. Paola Lanzafame and Dr. Georgia Papanikolaou (University of Messina) for chemical analysis via EDX.

Appendix A. Supplementary data

Supplementary material related to this article can be found, in the online version, at doi:https://doi.org/10.1016/j.apcatb.2018.10.060.

References

[1] A. Corma, State of the art and future challenges of zeolites as catalysts, J. Catal. 216

(2003) 298–312.
[2] J. Pérez-Ramírez, C.H. Christensen, K. Egeblad, C.H. Christensen, J.C. Groen, Hierarchical zeolites: enhanced utilisation of microporous crystals in catalysis by advances in materials design, Chem. Soc. Rev. 37 (2008) 2530–2542.
[3] D. Verboekend, J. Pérez-Ramírez, Design of hierarchical zeolite catalysts by desilication, Catal. Sci. Technol. 1 (2011) 879–890.
[4] Z. Qin, L. Lakiss, J.-P. Gilson, K. Thomas, J.-M. Goupil, C. Fernandez, V. Valtchev, Chemical equilibrium controlled etching of MFI-type zeolite and its influence on zeolite structure, acidity, and catalytic activity, Chem. Mater. 25 (2013) 2759–2766.
[5] M. Milina, S. Mitchell, P. Crivelli, D. Cooke, J. Pérez-Ramírez, Mesopore quality determines the lifetime of hierarchically structured zeolite catalysts, Nat. Comm. (2014) 3922.
[6] Z. Qin, J.-P. Gilson, V. Valtchev, Mesoporous Zeolites by Fluoride Etching Current Opinion in Chemical Engineering vol.8, (2015), pp. 1–6.
[7] M. Choi, K. Na, J. Kim, Y. Sakamoto, O. Teresaki, R. Ryoo, Stable single-unit-cell nanosheets of zeolite MFI as active and long-lived catalysts, Nature 461 (2009) 246–249.
[8] A. Corma, V. Fornes, S.B. Pergher, T.L. Maesen, J. Buglass, Delaminated zeolite precursors as selective acidic catalysts, Nature 396 (1998) 353.
[9] V. Valtchev, L. Tosheva, Porous nanosized particles: preparation, properties, and application, Chem. Rev. 113 (2013) 6734–6760.
[10] G. Yang, Y. Wei, S. Xu, J. Chen, J. Li, Z. Liu, J. Yu, R. Xu, Nanosize-enhanced lifetime of SAPO-34 catalysts in methanol-to-olefin reactions, J. Phys. Chem. C 117 (2013) 8214–8222.
[11] N. Nishiyama, M. Kawaguchi, Y. Hirota, D. Van Vu, Y. Egashira, K. Ueyama, Size control of SAPO-34 crystals and their catalyst lifetime in the methanol-to-olefin reaction, Appl. Catal. A: Gen. 362 (2009) 193–199.
[12] W. Dai, G. Wu, L. Li, N. Guan, M. Hunger, Mechanism of the deactivation of SAPO-34 materials with different crystal sizes applied as MTO catalysts, ACS Catal. 3 (2013) 588–596.
[13] D. Chen, K. Moljord, T. Fuglerud, A. Holmen, The effect of crystal size of SAPO-34 on the selectivity and deactivation of the MTO reaction, Microporous Mesoporous Mater. 29 (1999) 191–203.
[14] Y. Hirota, K. Murata, M. Miyamoto, Y. Egashira, N. Nishiyama, Light olefins synthesis from methanol and dimethyl ether over SAPO-34 nanocrystals, Catal. Lett. 140 (2010) 22–26.
[15] M. Firoozi, M. Baghalha, M. Asadi, The effect of micro and nano particle size of H-ZSM-5 on the selectivity of MTP reaction, Catal. Comm. 10 (2009) 1582–1585.
[16] H. Konno, T. Okumara, T. Kawahara, Y. Nakasaka, T. Tago, T. Masuda, Kinetics of n-hexane cracking over ZSM-5 zeolites-effect of crystal size on effectiveness factor and catalyst lifetime, Chem. Eng. J. 207 (2012) 490–496.
[17] M.V. Landau, L. Vradman, V. Valtchev, J. Lezervant, E. Liubich, M. Talianker, Hydrocracking of heavy vacuum gas oil with Pt/H-beta-Al_2O_3 catalyst: effect of zeolite crystal size in the nanoscale range, Ind. Eng. Chem. Res. 42 (2003) 2773–2782.
[18] M.A. Camblor, A. Corma, A. Martínez, V. Martínez-Soria, S. Valencia, Mild hydrocracking of vacuum gasoil over NiMo-Beta zeolite catalysts: the role of the location of the NiMo phases and the crystallite size of the zeolite, J. Catal. 179 (1998) 537–547.
[19] A. Martínez, C. López, The influence of ZSM-5 zeolite composition and crystal size on the in situ conversion of Fischer-Tropsch products over hybrid catalysts, Appl. Catal. A 294 (2005) 251–259.
[20] Y. Lee, M.B. Park, P.S. Kim, A. Vicente, C. Fernandez, I.-S. Nam, S.B. Hong, Synthesis and catalytic behavior of ferrierite nanoneedles, ACS Catal. 3 (2013) 617–621.
[21] P. Ratnasamy, G.P. Babu, A.J. Chandwadkar, S.B. Kilkarmi, Influence of crystal size of HZSM-5 on activity and shape selectivity in xylene isomerization, Zeolites 6 (1986) 98–100.
[22] A. Zheng, Z. Zhao, S. Chang, Z. Huang, H. Wu, X. Wang, F. He, H. Li, Effect of crystal size of ZSM-5 on the aromatic yield and selectivity from catalytic fast pyrolysis of biomass, J. Mol. Catal. A: Chem. 383 (2014) 23–30.
[23] T. Meng, D. Mao, Q. Guo, G. Lu, The effect of crystal sizes of HZSM-5 zeolites in ethanol conversion to propylene, Catal. Commun. 21 (2012) 52–57.
[24] C. Herrmann, J. Haas, F. Fetting, Effect of the crystal size on the activity of ZSM-5 crystals catalysts in various reactions, Appl. Catal. 35 (1987) 299–310.
[25] S. Mintova, J.-P. Gilson, V. Valtchev, Advance in nanosized zeolites, Nanoscale 5 (2013) 6693–6703.
[26] J. Grand, H. Awala, S. Mintova, Mechanism of zeolites crystal growth: new findings and open questions, Cryst. Eng. Comm. 18 (2016) 650–664.
[27] F. Di Renzo, Zeolites as tailor-made catalysts: control of the crystal size, Catal. Today 41 (1998) 37–40.
[28] V. Valtchev, S. Mintova, V. Dimov, A. Toneva, D. Radev, Tribochemical activation of seeds for rapid crystallization of zeolite Y, Zeolites 15 (1995) 193–197.
[29] X. Chen, T. Todorova, A. Vimont, V. Ruaux, Z. Qin, J.-P. Gilson, V. Valtchev, In situ and post-synthesis control of physicochemical properties of FER-type crystals, Microporous Mesoporous Mater. 200 (2014) 334–342.
[30] Y. Kamimura, K. Itabashi, T. Okubo, Seed-assisted, OSDA-free synthesis of MTW-type zeolite and "Green MTW" from sodium aluminosilicates gel systems, Microporous Mesoporous Mater. 147 (2012) 149–156.
[31] Q. Li, B. Mihailova, D. Creaser, J. Sterte, Aging effects on the nucleation and crystallization kinetics of colloidal TPA-silicalite-1, Microporous Mesoporous Mater. 43 (2001) 51–59.
[32] X. Zhang, D. Tang, G. Jiang, Synthesis of zeolite NaA at room temperature: the effect of synthesis parameters on crystal size and its size distribution, Adv. Powder Technol. 24 (2013) 689–696.
[33] K. Iwakai, T. Tago, H. Konno, Y. Nakasaka, T. Masuda, Preparation of nano-crystalline MFI zeolite via hydrothermal synthesis in water/surfactant/organic solvent using fumed silica as Si source, Microporous Mesoporous Mater. 141 (2011) 167–174.
[34] T. Tago, D. Aoki, K. Iwakai, T. Masuda, Preparation for size-controlled MOR zeolite nanocrystal using water/surfactant/organic solvent, Top. Catal. 52 (2009) 865–871.
[35] N.L. Chauhan, J. Das, R.V. Jasra, Z.V.P. Murthy, P.A. Parikh, Synthesis of zeolite ZSM-5: effect of emulsifiers, Cryst. Res. Technol. 47 (2012) 746–753.
[36] N.L. Chauhan, Z.V.P. Murthy, J. Das, P.A. Parikh, Synthesis of zeolite ferrierite-role of emulsifiers, Indian J. Chem. Technol. 18 (2011) 335–342.
[37] E. Catizzone, A. Aloise, M. Migliori, G. Giordano, Dimethyl ether synthesis via methanol dehydration: effect of zeolite structure, Appl. Catal. A 502 (2015) 215–220.
[38] E. Catizzone, A. Aloise, M. Migliori, G. Giordano, From 1-D to 3-D zeolite structures: performances assessment in catalysis of vapour-phase methanol dehydration to DME, Microporous Mesoporous Mater. 243 (2017) 102–111.
[39] E. Catizzone, M. Migliori, A. Purita, G. Giordano, Ferrierite vs. γ-Al2O3: the superiority of zeolites in terms of water-resistance in vapour-phase dehydration of methanol to dimethyl ether, J. Energy Chem. (2018), https://doi.org/10.1016/j.jechem.2018.05.004.
[40] G. Bonura, F. Frusteri, C. Cannilla, G. Drago Ferrante, A. Aloise, E. Catizzone, M. Migliori, G. Giordano, Catalytic features of CuZnZr-zeolite hybrid systems for the direct CO_2-to-DME hydrogenation reaction, Catal. Today 277 (2016) 48–54.
[41] F. Frusteri, M. Migliori, C. Cannilla, L. Frusteri, E. Catizzone, A. Aloise, G. Giordano, G. Bonura, Direct CO2-to-DME hydrogenation reaction: new evidences of a superior behaviour of FER-based hybrid systems to obtain high DME yield, J. CO_2 Util. 18 (2017) 353–361.
[42] G. Bonura, M. Migliori, L. Frusteri, C. Cannilla, E. Catizzone, G. Giordano, F. Frusteri, Acidity control of zeolite functionality on activity and stability of hybrid catalysts during DME production via CO_2 hydrogenation, J. CO_2 Util. 24 (2018) 398–406.
[43] E. Catizzone, G. Bonura, M. Migliori, F. Frusteri, G. Giordano, CO_2 recycling to dimethyl ether: state-of-the-art and perspectives, Molecules 23 (2018) 31–58.
[44] G. Centi, S. Perathoner, Opportunities and prospects in the chemical recycling of carbon dioxide to fuels, Catal. Today 148 (2009) 191–205.
[45] Z. Azizi, M. Rezaeimanesh, T. Tohidian, M.R. Rahimpour, Dimethyl ether: a review of technologies and production challenges, Chem. Eng. Process. 82 (2014) 150–172.
[46] E. Catizzone, A. Aloise, M. Migliori, G. Giordano, The effect of FER zeolite acid sites in methanol-to-dimethyl ether catalytic dehydration, J. Energy Chem. 26 (2017) 406–415.
[47] A.A. Rownaghi, F. Rezaei, M. Stante, J. Hedlund, Selective dehydration of methanol to dimethyl ether on ZSM-5 nanocrystals, Appl. Catal. B: Environ. 119 (2012) 56–61.
[48] A. Aloise, E. Catizzone, M. Migliori, J.B. Nagy, G. Giordano, Catalytic behaviour in propane aroamtization using Ga-MFI catalyst, Chin. J. Chem. Eng. 25 (2017) 1863–1870.
[49] M. Migliori, A. Aloise, E. Catizzone, G. Giordano, Kinetic analysis of methanol to dimethyl ether reaction over H-MFI catalyst, Ind. Eng. Chem. Res. 53 (2014) 14885–14891.
[50] A. Bonilla, D. Baudouin, J. Perez-Ramírez, Desilication of ferrierite zeolite for porosity generation and improved effectiveness in polyethylene pyrolisis, J. Catal. 265 (2009) 170–180.
[51] A.A. Rownaghi, F. Rezaei, J. Hedlund, Uniform mesoporous ZSM-5 single crystals catalyst with high resistance ton coke formation for methanol deoxygenation, Microporous Mesoporous Mater. 151 (2012) 26–33.
[52] G. Leofanti, M. Padovan, G. Tozzola, B. Venturelli, Surface area and pore texture of catalysts, Catal. Today. 4 (1998) 207–219.
[53] A.A. Rownaghi, J. Hedlund, Methanol to gasoline-range hydrocarbons: influence of nanocrystal size and mesoporosity on catalytic performances and product distribution of ZSM-5, Ind. Eng. Chem. Res. 50 (2010) 11872–11878.
[54] A.A. Rownaghi, F. Rezaei, J. Hedlund, Yield of gasoline-range hydrocarbons as a function of uniform ZSM-5 crystal size, Catal. Comm. 14 (2011) 37–41.
[55] M. Trombetta, T. Armaroli, A.G. Alejandre, J.R. Solis, G. Busca, An FT-IR study of the internal and external surfaces of HZSM5 zeolite, Appl. Catal. A: Gen. 192 (2000) 125–136.
[56] Y.P. Khitev, Y.G. Kolyagin, I.I. Ivanova, O.A. Ponomareva, F. Thibault-Starzyk, J.-P. Gilson, C. Fernadez, F. Fajula, Synthesis and catalytic properties of hierarchical micro/mesoporous materials based on FER zeolite, Microporous Mesoporous Mater. 146 (2011) 201–207.
[57] J. Datka, M. Kawalek, K. Góra-Marek, Acid properties of NaKH-ferrierites of various exchange degrees studied by IR spectroscopy, Appl. Catal. A: Gen. 243 (2003) 293–299.
[58] P. Cañozares, A. Carrero, P. Sánchez, Isomerization of n-butene over ferrierite zeolite modified by silicon tetrachloride treatment, Appl. Catal. A: Gen. 190 (2000) 93–105.
[59] D.P.B. Peixoto, S.M. Cabral de Menezes, M.I.Pais da Silva, Influence of different processes of dealumination on acid properties of an H-ferrierite zeolite, Mater. Lett. 57 (2003) 3933–3942.
[60] B. Wichterlová, Z. Tvarůková, Z. Sobalík, P. Sarv, Determination and properties of acid sites in H-ferrierite: a comparison of ferrierite and MFI structures, Microporous Mesoporous Mater. 24 (1998) 223–233.
[61] C. Pazé, A. Zecchina, S. Spera, G. Spano, F. Rivetti, Acetonitrile as probe molecule for an integrated ^{1}H NMR and FTIR study of zeolitic Brønsted acidity: interaction with zeolites H-ferrierite and H-beta, Phys. Chem. Chem. Phys. 2 (2000) 5756–5760.

[62] S. van Donk, E. Bus, A. Broersma, J.H. Bitter, K.P. de Jong, Probing the accessible sites for n-butene skeletal isomerization over aged and selective H-ferrierite with d_3-acetonitrile, J. Catal. 212 (2002) 86–93.
[63] P.A. Jacobs, C.F. Heylen, Active sites in zeolites, J. Catal. 34 (1974) 267–274.
[64] C. Morterra, G. Cerrato, G. Meligrana, Revisiting the use of 2,6-dimethylpyridine adsorption as probe molecule for the acidic properties of metal oxides, Langmuir 17 (2001) 7053–7060.
[65] F. Thibault-Starzyk, I. Stan, S. Abellò, A. Bonilla, K. Thomas, C. Fernandez, J.-P. Gilson, J. Perez-Ramírez, Quantification of enhanced acid site accessibility in hierarchical zeolites – the accessibility index, J. Catal. 264 (2009) 11–14.
[66] T. Onfroy, G. Clet, M. Houalla, Quantitative IR characterization of the acidity of various oxide catalysts, Microporous Mesoporous Mater. 82 (2005) 99–104.
[67] K. Sadowska, K. Góra-Marek, J. Datka, Accessibility of acid sites in hierarchical zeolites: quantitative IR studies of pivalonitrile adsorption, J. Phys. Chem. C 117 (2013) 9237–9244.
[68] T. Montanari, M. Bevilacqua, G. Busca, Use of nitrile sas probe molecules for the accessibility of the active sites and the detection of complex interactions in zeolites through IR spectroscopy, Appl. Catal. A: Gen. 307 (2006) 21–29.
[69] M. Cai, A. Palčić, V. Subramanian, S. Moldovan, O. Ersen, V. Valtchev, V.V. Ordomsky, A.Y. Khodakov, Direct dimethyl ether synthesis from syngas on copper-zeolite hybrid catalysts with a wide range of zeolite particle size, J. Catal. 338 (2016) 227–238.
[70] M. Boudart, Turnover rates in heterogeneous catalysis, Chem. Rev. 95 (1995) 661–666.
[71] M. Bjørgen, S. Svelle, F. Joensen, J. Nerlov, S. Kolboe, F. Bonino, L. Palumbo, S. Bordiga, U. Olsbye, Conversion of methanol to hydrocarbons over zeolite H-ZSM-5: on the origin of the olefinic species, J. Catal. 249 (2007) 195–207.
[72] P. Tian, Y. Wei, M. Ye, Z. Liu, Methanol to olefins (MTO): from fundamentals to commercialization, ACS Catal. 5 (2015) 1922–1938.
[73] J.F. Haw, W. Song, D.M. Marcus, J.B. Nicholas, The mechanism of methanol to hydrocarbon catalysis, Acc. Chem. Res. 36 (2003) 317–326.
[74] M. Stöcker, Methanol-to-hydrocarbons: catalytic materials and their behavior, Microporous Mesoporous Mater. 29 (1999) 3–48.
[75] K.P. Möller, W. Böhringer, A.E. Schnitzler, E. van Steen, C.T. O'Connor, The use of a jet loop reactor to study the effect of crystal size and the co-feeding of olefins and water on the conversion of methanol over ZSM-5, Microporous Mesoporous Mater. 29 (1999) 127–144.
[76] M. Guisnet, P. Magnoux, Organic chemistry of coke formation, Appl. Catal. A: Gen. 212 (2001) 83–96.
[77] U. Olsbye, S. Svelle, M. Bjørgen, P. Beato, T.V.W. Janssens, F. Joensen, S. Bordiga, K.P. Lillerud, Conversion of methanol to hydrocarbons: how zeolite cavity and pore size controls product selectivity, Angew. Chem. 51 (2012) 5810–5831.
[78] X.-J. Liu, Y.-D. Zhang, L. Sun, W.-Q. Deng, Computational screening of zeolite catalysts for MTO reaction, ChemistrySelect 2 (2017) 10290–10294.